Dynamics and regulation at the tip : a high resolution view on microtubele assembly

Munteanu, L.

CHAPTER

3 Influence of XMAP215 on microtubule dynamics

XMAP215 is a microtubule-associated protein that is known to dramatically enhance the microtubule growth velocity. The molecular mechanism by which this effect is achieved is not yet understood. We used optical tweezers to observe the assembly dynamics of individual microtubules at molecular resolution. We find that microtubules can near-instantaneously increase their overall length by amounts exceeding the size of individual dimers (8 nanometer). When the microtubule-associated protein XMAP215 is added, this effect is dramatically enhanced and fast length increases around 60 nanometer are observed (which corresponds to the length of the XMAP215 protein itself). The enhanced addition of tubulin at the growing end of the microtubule in the presence of XMAP215 can have several interpretations: The XMAP215 protein might act as a template to assemble long tubulin oligomers, either in solution or at the microtubule tip. In order to further shed light on the molecular mechanism of interaction between tubulin and XMAP215 we used fluorescence speckle microscopy and fluorescence correlation spectroscopy. In these experiments we attempted to measure XMAP215-tubulin complex formation. We did not detect big size complexes that would correspond to the full length of XMAP215 protein covered with tubulin dimers. Therefore, the fast length increases observed during microtubule growth at high resolution, might be due to a local acceleration of tubulin dimer addition when XMAP215 is present at the microtubule end. Further experiments are necessary to elucidate the molecular mechanism of interaction between XMAP215 and tubulin.

Microtubules are highly dynamic protein polymers [6] that form a crucial part of the cytoskeleton in all eukaryotic cells. The core structure of a microtubule consists of typically 13 or 14 protofilaments forming a hollow tube (Figure 3.1 a). Microtubule assembly is accompanied by the hydrolysis of tubulin-bound GTP, which occasionally triggers the microtubule to undergo a catastrophe and switch to a state of rapid disassembly [6]. Information about the structure of growing and shrinking microtubule ends as well as the (preferred) conformational state of GTP-bound and GDP-bound tubulin in these situations comes from static electron microscopy studies [34, 50, 51], which indicate that growing microtubule ends consist of sheets of slightly outward-curved protofila-

ments and that shrinking microtubule ends consist of individual protofilaments that curve outwards more strongly. Information on the assembly dynamics of microtubules has been limited, both *in vitro* [56, 57] and *in vivo* [54, 55] to measurements of average growth and shrinkage rates over several thousands of tubulin subunits.

To obtain dynamic information on the growth and shrinkage of microtubules at the resolution of single tubulin dimers (8 nm) we used a technique based on optical tweezers (chapter 2). We show results for microtubule assembly from pure tubulin, and then show how, on a molecular scale, the growth process is altered by the presence of XMAP215, an evolutionary conserved protein [120] that enhances the growth rate of microtubules [121, 122, 153].

3.1 Microtubule assembly in the presence of XMAP215

3.1.1 XMAP215 enhances microtubule growth and catastrophes

To test the effect of XMAP215 on the dynamics of freely growing microtubules, we followed the growth and shrinkage of microtubules nucleated from axonemes and seeds (short stable microtubules) using DIC microscopy (see section 3.3.1).

The changes in the dynamic instability parameters in the presence of XMAP215 are summarized in table 3.1. As expected from previous observations [121, 122], XMAP215 had a potent effect on the microtubule growth velocity. The growth speed enhancement was stronger with increasing XMAP215 concentration. Microtubules grew 4 times faster when XMAP215 was present in solution at a ratio of 1 : 20 XMAP215 : tubulin. XMAP215 had also a destabilizing effect on microtubules by stimulating catastrophes and increasing the shrinkage speed. This effect can not be explained only by the presence in the sample of extra salts from the protein buffer, which also induced destabilization of microtubules. In the presence of XMAP215 the increase in the catastrophe rate was stronger. We also observed that XMAP215 induces depolymerization of the GMPCPP stabilized microtubules, used as nucleation sites in these experiments. The depolymerization of GMPCPP microtubules by XMAP215 was also reported earlier [68]. XMAP215 was proposed to destabilize the microtubule 'blunt' ends (that are believed to represent a paused microtubule state), which would increase the chance of transition to the shrinkage phase.

It is still not known how XMAP215 can exert a dual effect on microtubule dynamics. It is possible that the protein can enhance both the on- and off-rate of GTP-tubulin assembly at the growing microtubule tip. Depending on the conditions, either microtubule growth or catastrophes would be favored. To find more information on the mechanism by which XMAP215 influences the microtubule growth dynamics, we followed microtubule assembly process at molecular resolution.

tub [μM]	XMAP215 [nM]	buffer (+/-)	v_{gro} (μm/min) mean ± sem (n)	v_{shr} (μm/min) mean ± sem (n)	f_{cat} (min^{-1}) mean ± sd (N_{cat})
10	0	-	0.58 ± 0.02 (24)	19 ± 2 (18)	0.19 ± 0.04 (21)
15	0	-	0.91 ± 0.19 (64)	18 ± 1 (23)	0.16 ± 0.02 (63)
20	0	-	1.08 ± 0.04 (27)	22 ± 1 (21)	0.13 ± 0.03 (23)
25	0	-	1.24 ± 0.05 (15)	10 ± 1 (9)	0.07 ± 0.02 (13)
15	0	+	0.91 ± 0.03 (44)	29 ± 1 (44)	0.35 ± 0.05 (47)
15	150	+	1.40 ± 0.12 (8)	46 ± 3 (6)	0.60 ± 0.21 (8)
15	255	+	1.49 ± 0.07 (21)	38 ± 4 (16)	0.71 ± 0.15 (24)
15	675	+	3.78 ± 0.39 (16)	25 ± 3 (13)	1.40 ± 0.35 (16)
				$t_{cat} = \langle L \rangle / v_{gro}$ (sec)	MT end
20	0	+	1.70 ± 0.14 (8)	–	plus
20	150	+	2.30 ± 0.30 (11)	140	plus
20	0	+	0.30 ± 0.05 (5)	–	minus
20	150	+	1.00 ± 0.15 (4)	500	minus

Table 3.1: Dynamic instability parameters of microtubules growing freely from seeds (upper half) or axonemes (lower half) were measured. Growth velocities, v_{gro}, were measured as linear fits to individual growth events (total n). Shrinkage velocities were measured in a similar way from the moment a catastrophe occurred until the microtubule disappeared (no rescues were observed). Errors represent s.e.m. The catastrophe frequency, f_{cat}, was calculated by dividing the total number of catastrophes observed, N_{cat}, by the total growth time. The errors were evaluated as $f_{cat}/\sqrt{N_{cat}}$. For the microtubules nucleated by axonemes an estimate for the average catastrophe time, t_{cat}, is given as the average microtubule length over the entire observation time, $\langle L \rangle$, divided by the growth velocity, v_{gro}. Minus ends had very few catastrophes, even in the presence of XMAP215.

3.1.2 Assembly dynamics at molecular resolution

To follow dynamic microtubules with high-resolution, we used a method based on optical tweezers (chapter 2). The experimental set-up is shown schematically in figure 3.1 b. Shortly, we allowed dynamic microtubule plus ends to grow and shrink against a microfabricated barrier and we monitored the response of a microbead attached at the other end of the microtubule nucleation site, an axoneme. The bead-axoneme construct was held by a 'keyhole' optical trap.

Figure 3.1 c shows the restoring force exerted by the trap during a sequence of microtubule growth and shrinkage events. The upper panel shows regular microtubule growth, with an initial tubulin concentration of 20 μM. The protein concentration slowly decreases as indicated by the smooth curves (as the result of a slow buffer flow). Growth often comes to an apparent halt at a few piconewtons of force before catastrophes occur, which is consistent with what is known for the effect of force on the assembly dynamics of microtubule plus ends [70, 76, 77]. The frequent occurrence of catastrophes confirms that the observed growth is that of a plus end of a microtubule. The

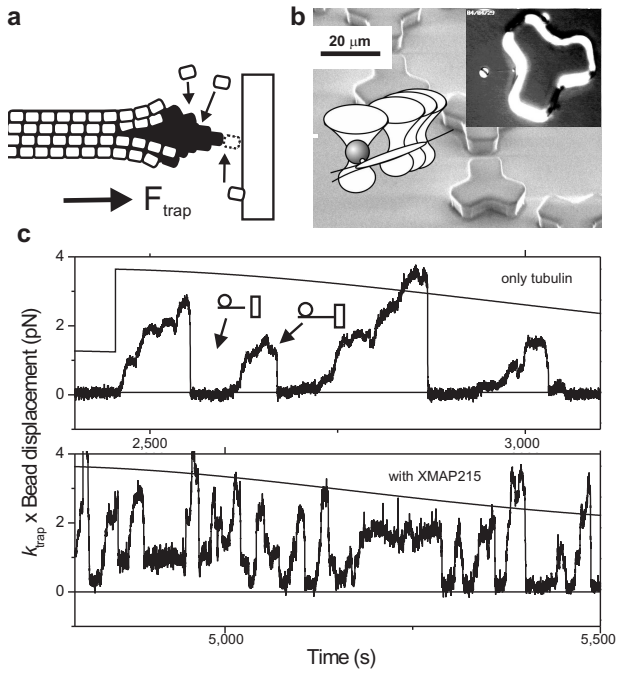

Figure 3.1: Measuring growth dynamics of microtubules with optical tweezers. **(a)** Schematic view of a growing microtubule. **(b)** Schematic and DIC image of a 'keyhole' optical trap holding a bead-axoneme construct in front of a microfabricated barrier. **(c)** Growth and shrinkage events of individual microtubules in the absence (upper panel) and presence (lower panel) of XMAP215. The smooth curves give estimates of the gradually decreasing protein concentration (maximum tubulin concentration 20 μM).

lower panel shows growth from the same construct after replacement of the surrounding solution with 20 μM tubulin and 150 nM XMAP215. With XMAP215 present, growth is faster and catastrophes occur more frequently, in agreement with previous reports [68, 121, 122, 153] and our own observations in the absence of force (section 3.1.1).

Figure 3.2 shows part of the same data at higher resolution, this time with the microtubule length, corrected for the stiffness of the bead-axoneme construct, on the y axis. These data gives us unprecedented resolution on the growth dynamics of individual microtubules, limited only by the thermal noise on the bead in the trap and the stiffness of the bead-axoneme construct (about 5-10 nm root-mean-square in practice). In these data we occasionally observe step-like length increases that are clearly distinguishable from the experimental noise, even by eye (figure 3.2 a, arrows). When we add XMAP215 (figure 3.2 b), fast increases occur more frequently and are also larger, on the order of several tens of nanometers, occurring on a timescale of about 100 ms or less (the average microtubule growth rate under these conditions corresponds to at most

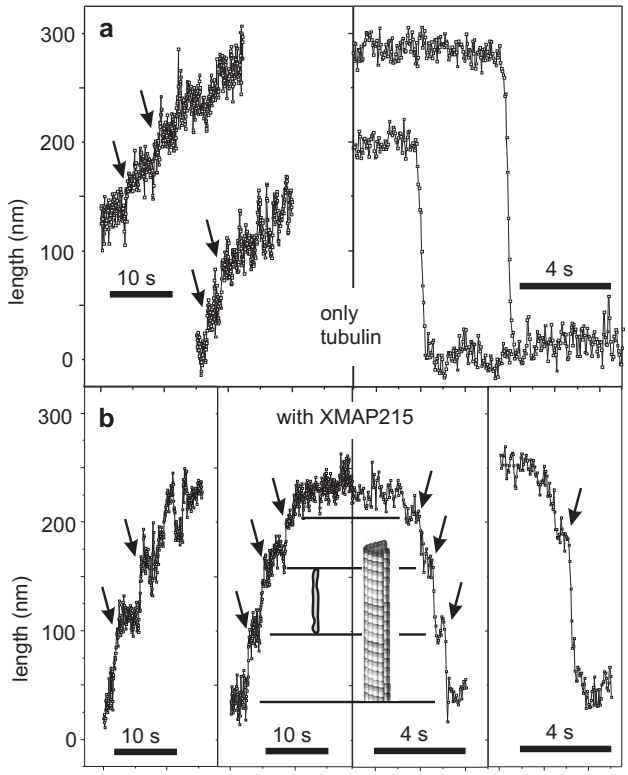

Figure 3.2: High-resolution details of growth and shrinkage events. Length traces are shown for events without **(a)** and with **(b)** XMAP215. Arrows indicate fast length changes (steps) that are distinguishable from the noise by eye. During subsequent growth and shrinkage events in the presence of XMAP215, steps sometimes appear in register with each other (**(b)**, middle, lines). The insets show schematic drawings of an XMAP215 molecule (left) and a microtubule (right) at the same scale as the length data.

1 or 2 nm per 100 ms). In the presence of XMAP215, steps are also clearly observed during shrinkage events (figure 3.2 b, right). These steps are of similar sizes to those observed during growth, sometimes even in marked registry with previous growth steps (figure 3.2 b, middle). The sizes of the large steps often seem close to the known length of the XMAP215 protein itself [64], as indicated in figure 3.2 b. In addition to steps we observe periods with more gradual increases in length, in which steps are not clearly distinguishable. Given our experimental resolution this is to be expected: microtubule ends are likely to have multiple binding sites for tubulin dimers at unequal positions along the microtubule axis (see figure 3.1 a), and growth due to single dimer additions, for example, should lead to mostly small steps with a maximum of 8 nm.

To be able to analyze in an unbiased way the steps observed by eye, we developed

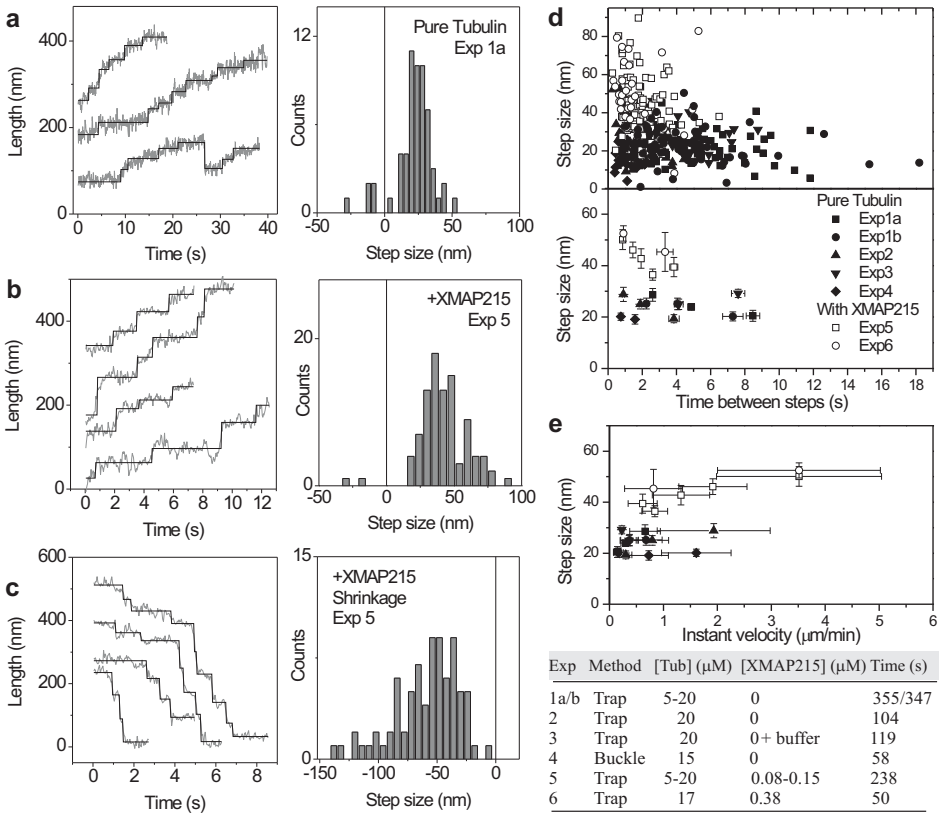

Exp	Method	[Tub] (μM)	[XMAP215] (μM)	Time (s)
1a/b	Trap	5-20	0	355/347
2	Trap	20	0	104
3	Trap	20	0+ buffer	119
4	Buckle	15	0	58
5	Trap	5-20	0.08-0.15	238
6	Trap	17	0.38	50

Figure 3.3: Quantifying the sizes of the large steps with our step-fitting algorithm. Step fits and associated step histograms are shown for regular microtubule growth **(a)**, growth with XMAP215 present **(b)** and shrinkage with XMAP215 present **(c)**. **(d)** Step sizes for six different growth experiments with conditions and analyzed growth times as listed in the table (experiments 1a, 1b and 5 were performed with the same bead-axoneme construct; shrinkage was analyzed only for experiment 5 (63 s); experiment 4 involves data obtained previously with a different 'buckling' method [76]). Top: individual step sizes plotted against the time between steps. Bottom: the same data averaged over 20 steps (the last data point may contain fewer steps). **(e)** Averaged step sizes as in **(d)** but plotted against 'instant velocity' (step size divided by time between steps). Error bars in **(d)** and **(e)** represent s.e.m.

a step-fitting algorithm as outlined in section 3.3.2. Because in our system many of the steps were smaller than the noise, we could use the algorithm only to find and quantify the largest steps (figure 3.3). In the histograms presented, any steps (or lack thereof) close to or below the noise level are therefore insignificant. For regular tubulin growth, the step fit result and the associated histogram (figure 3.3 a) confirm the presence of steps up to 20 - 30 nm in size. This is significantly larger than the tubulin dimer size of 8 nm. In the presence of XMAP215, the histograms for growth (figure 3.3 b) and shrink-

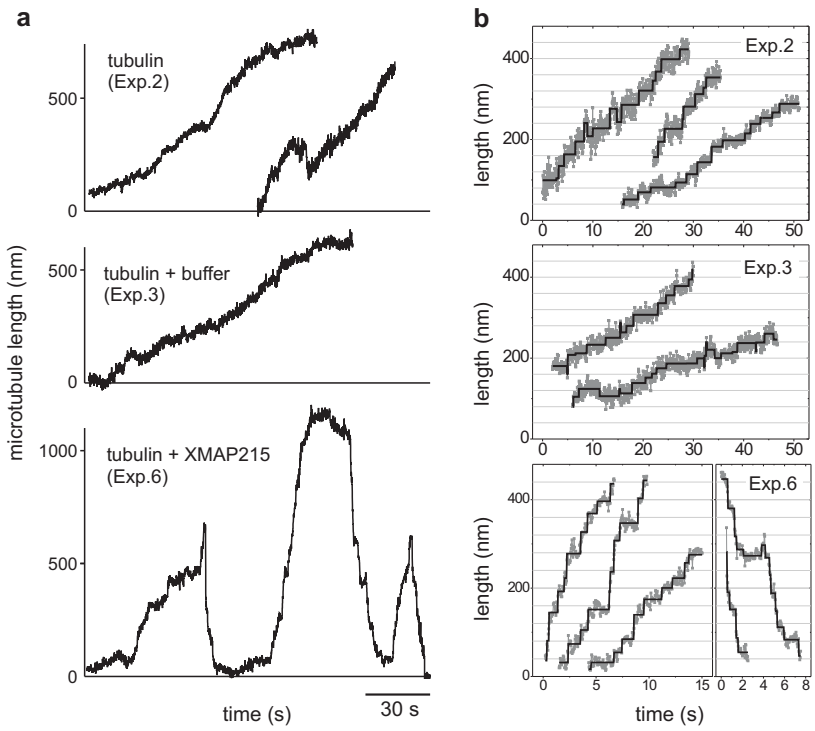

Figure 3.4: Microtubule growth and shrinkage events. **(a)** Length traces of microtubules assembled in the absence (upper panel, experiment 2), in the presence of protein buffer (middle panel, experiment 3), and in the presence of XMAP215 (lower panel, experiment 6) were monitored.The protein concentrations used in these experiments are listed in table in figure 3.3 e. In the experiments without XMAP215 we did not detect catastrophes as the growing microtubule(s) later adhered with the tip non-specifically to the photoresist wall that prevented them from depolymerization. **(b)** Part of the same data at higher resolution and the step fit result. The starting point of each segment (both length and time) is relative.

age (figure 3.3 c) show larger step-like changes, around 40 - 60 nm in size. The observed step sizes are independent of how quickly steps follow each other (i.e. the rate at which microtubules grow). Our experiments were performed at various tubulin concentrations and forces (both of which affect the average microtubule growth velocity [76]), as well as for two different XMAP215/tubulin ratios. When we plot individual (figure 3.3 d, top) and averaged (figure 3.3 d, bottom) step sizes as a function of the time between steps for six different experiments, we find that the step sizes are always larger in the presence of XMAP215, even when the resulting (instant) growth velocity is the same (plotted in figure 3.3 e). Figure 3.4 shows microtubule growth traces from the experiments used to evaluate step sizes, other than the data included in figure 3.3 a-c (see table in figure 3.3 e).

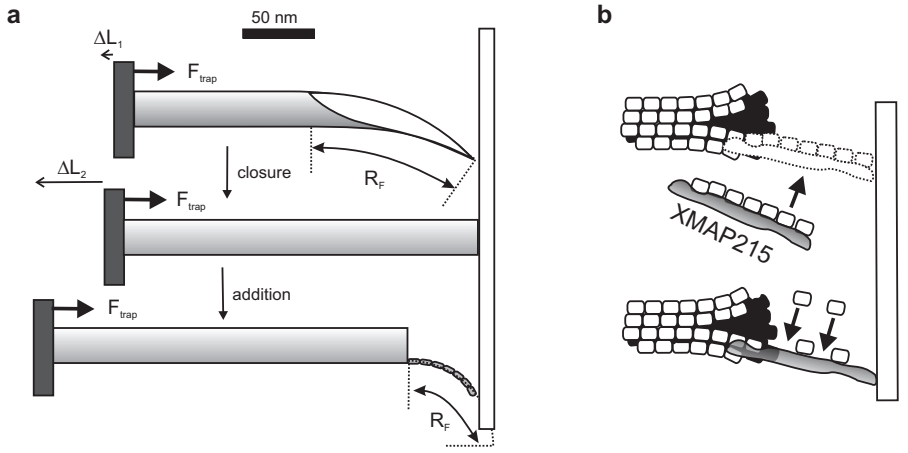

Figure 3.5: Microtubule end mechanics. (a) Schematic drawing of a microtubule end under a compressive force (roughly to scale). Top: a microtubule with a sheet-like extension of 125 nm (preferred radius of curvature $R_0 \approx 250$ nm) adopts a force-induced radius of curvature $R_F \approx 200$ nm under a compressive force of 2.5 pN (conservative estimate of the sheet stiffness 1.2×10^5 pN nm^2; that is, about 1/100 that of a microtubule). Middle: the same microtubule appears about 8 nm longer (ΔL_1) on full sheet closure. Bottom: the addition of a single, 60-nm-long protofilament (preferred radius of curvature 76 nm; stiffness 2.4×10^4 pN nm^2) under a similar compressive force will lead to an apparent length increase (ΔL_2) of about 50 nm ($R_F \approx 60$ nm). **(b)** Possible mechanisms for XMAP215-enhanced addition of long oligomers.

3.2 Discussion

The observation of fast increases in length larger than the dimer size might have two interpretations: either we were observing extended closure events of outward-curved sheets existing at the ends of growing microtubules, or we were observing the addition of tubulin oligomers larger than individual tubulin dimers. To estimate the expected length increase in these two cases, we must consider the geometry and rigidity of tubulin oligomers and microtubule sheets as well as the distortions that one expects in the presence of a few piconewtons of force. In our experiments microtubules grew relatively slowly and never very long (typically a few hundred nanometers). In figure 3.5 a we show schematically a reasonable estimate, based on electron microscopy studies [34, 154], of a typical microtubule sheet under these conditions, drawn to scale. The estimates shown in figure 3.5 (see also section 3.3.1) indicate that length increases due to oligomer addition, as opposed to sheet closure events, should be readily detectable.

Our observations therefore indicate that microtubule assembly might not always occur simply by the addition of individual tubulin dimers. Small oligomers of up to three tubulin dimers seem to be able to attach to growing microtubules as well. This is consistent with observations that microtubule assembly is reduced when tubulin oli-

gomers are centrifuged away from microtubule polymerization solutions [51]. The step sizes of 40 - 60 nm in the presence of XMAP215 indicate that XMAP215 might facilitate the addition of even longer oligomers. Again, there are two ways in which this could be accomplished [63, 65]. First, XMAP215 could template the assembly of a tubulin oligomer in solution and this whole complex could subsequently attach to the end of the growing microtubule (figure 3.5 b, top). Because the overall growth velocity of microtubules is enhanced by the addition of even a small amount of XMAP215, this would have to mean that the XMAP215-tubulin complex has a higher affinity for the microtubule end than tubulin alone (possibly because of 'pre-straightening' of the tubulin oligomer by the XMAP215 molecule). To us, this seems a likely mechanism because it is known from electron microscopy studies that XMAP215 can bind free tubulin dimers in a protofilament-like fashion, resulting in XMAP215-tubulin complexes with lengths up to 60 nm [64]. In addition, there is indirect evidence that other microtubule-binding proteins such as CLIP170 bind tubulin dimers before attaching to growing microtubules as well [29, 66, 67].

The second possibility is that XMAP215 could first bind to the microtubule end and then accelerate the build-up of an oligomer along the length of the XMAP215 molecule (figure 3.5 b, bottom). In both cases it is possible that the XMAP215-tubulin complex first binds under an angle to the microtubule end and then straightens out the longitudinal bond in some kind of power stroke. In fact, the instant straight addition of an oligomer 40 - 60 nm long through a purely brownian ratchet mechanism would require an unusually large fluctuation of the microtubule end away from the barrier [76]. Finally, the step-like nature of shrinkage events indicates that XMAP215 might stay attached to the microtubule lattice for at least some time after arrival, where it hampers microtubule depolymerization. The shrinkage phases are further discussed in chapter 6.

The method described here for detecting the molecular details of microtubule assembly also paves the way for understanding the action of other classes of microtubule associated proteins [20,22,155]. Microtubule-associated proteins and end-binding proteins mediate the interaction of microtubules with cellular targets such as the kinetochore and the cell cortex. Understanding, at a molecular level, the operating principles of these proteins will be essential for understanding the regulation of microtubule dynamics in cells.

3.3 Methods

3.3.1 Measuring microtubule dynamics

DIC measurements on freely growing microtubules. Dynamic microtubules were nucleated from stabilized seeds or axonemes. The stabilized seeds were prepared by incubation of a tubulin mix containing biotin-labelled and non-labelled tubulin (Cytoskeleton) in a ration of 1:5 (total of 100 μM tubulin) with 1 mM GMPCPP (Jena Bioscience) at

36^{o}C for 30-60 minutes. The biotin-labelled seeds were specifically bound to a streptavidin functionalized surface in a flow chamber. The surface was realized by incubating the chamber with 2.5 mg/ml biotin-BSA in acetate buffer (21 mM acetic acid, 79 mM $C_2H_3O_2Na$, pH 5.2) and after rinsing, subsequent incubation with 1 mg/ml streptavidin in assay buffer (MRB80, pH 6.8). All chemicals were purchased from Sigma, otherwise mentioned. The axonemes, the same as used for the trap experiment, were directly bound to the pre-cleaned glass coverslip by non-specifically interactions and the surface was subsequently passivated by incubation with 10 mg/ml BSA. Microtubules were imaged by video-enhanced differential interference contrast (VE-DIC) microscopy for 60-90 min. Movies of the experiments were recorded on video tape and digitized offline at a rate of 2 Hz. Microtubule length versus time traces were measured using an inhouse developed software written and run in IDL. Growth and shrinkage speeds were evaluated from individual events by a linear fit. More details about the sample preparation and the data analysis are given for a similar experiment in section 5.5.1.

Optical tweezers based technique (see chapter 2 for details). We used an Nd:YVO4 1064-nm laser (Spectra Physics) to trap a construct: a bead connected to a rigid axoneme (figure 3.1 b). The laser was time-shared to create a 'keyhole' trap [142], consisting of a point trap holding the bead and a line trap directing the axoneme towards a microfabricated barrier. Photoresist (SU-8) barriers [144] were made using standard microlithography techniques. Axonemes from sea urchin sperm were prepared by M. Footer from published protocols [146] and were bound to streptavidin-coated beads (2 μm diameter, Spherotech) by non-specific binding. Microtubule growth was initiated by flowing in a mixture of tubulin and GTP, with or without the addition of XMAP215. The conditions were chosen such that most of the time only one or two microtubules were nucleated by the plus end of the axoneme. When a microtubule reached the barrier, further length increases led to displacement of the bead in the trap. The relation between the increase in microtubule length and the displacement of the bead depends on the stiffness of the bead-axoneme construct, which we measured independently by pushing the barrier against the construct (figure 3.6 a) before growth was initiated. Displacement of the bead in the optical trap led to an increasing restoring force on the bead (given by the trap stiffness, k_{trap}, multiplied by the bead displacement) that pushes the growing microtubule tip against the barrier. We kept the growing microtubule short (less than 1 μm) to prevent the microtubule from buckling under this compressive load [70]. DIC images of our experiments were recorded on DVD with a charge-coupled device camera (Kappa) and a standard DVD recorder (Philips DVD-R80). The displacement of the bead in the trap was measured from the digital images at a sampling rate of 25 Hz with the use of a standard auto-correlation method (image processing software home-written in IDL).

A step-fitting algorithm was developed and written in MatLab (section 3.3.2). To test how well our set-up is able to distinguish stepped from linear growth and to verify that

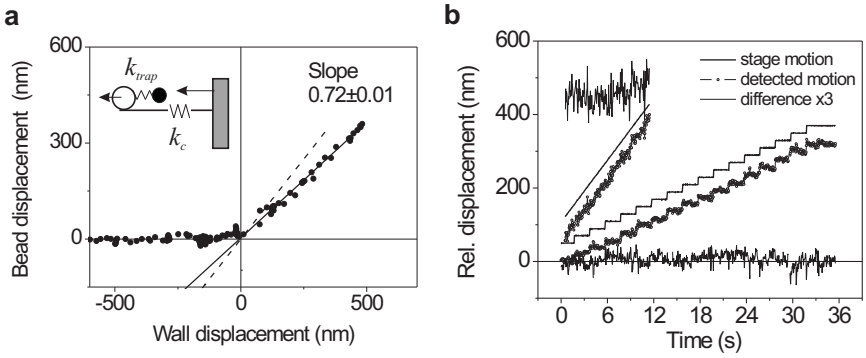

Figure 3.6: Step detection test. **(a)** Measurement of the construct compliance by a bouncing procedure: repeatedly pushing the wall against the construct and monitoring the bead response as a function of the wall displacement. In the linear regime, the slope of this plot is given by $\Delta_{\text{bead}}/\Delta_{\text{wall}} = k_c/(k_c+k_{\text{trap}})$. The dotted line indicates a slope of 1. **(b)** Trap measurements (small open circles) of piezo-stage-induced linear and stepped motions of the wall against the axoneme tip (solid lines). The thin solid lines depict 3-fold enhanced difference signals.

no artificial steps are introduced or detected, we pushed the wall against the construct in a linear, as well as in a stepped manner using a piezo stage. We recorded the bead displacement, corrected for the construct stiffness and compared the detected motion with the wall motion (figure 3.6 b). We used steps of 20 nm and the speed was chosen to be in the range of typical microtubule growth speeds, on the order of 1 μm/min. The solid lines depict the programmed motion of the piezo stage. The open circles indicate the response of the bead, after the linear correction. The difference between the detected motion and the wall motion (thin solid lines, magnified by a factor 3) shows no significant features that can be interpreted as steps of several tens of nanometer as observed in the microtubule growth experiments. On the other hand, the purposely-introduced steps of 20 nm are all correctly detected.

Microtubule growth. Microtubule growth was initiated by flowing tubulin into the sample, which was kept at a constant temperature of 25 ± 1°C. Growth solutions contained MRB80 buffer (80 mM K-Pipes, 1 mM EGTA, 4 mM $MgCl_2$, pH 6.8) + 250 μM GTP, and 5-10 mg/ml BSA. Growth solutions with XMAP215 additionally contained small amounts of Tris, Bis-Tris-propane, NaCl, DTT, and glycerol (resp. 0.8 mM, 0.8 mM, 26.4 mM, 80 μM, and 0.8% in Exp 5 and 0.7 mM, 0.7 mM, 5.5 mM, 16 μM, and 0.16% in Exp 6) and some protease inhibitors. Exp 3 in figure 3.3 and 3.4 (the control with buffer) contains data with very similar buffer additions. Recombinant XMAP215 was expressed in Sf+ insect cells, purified as described previously [153] and stored in liquid nitrogen. The protein concentration was determined with a Bradford assay and the molar extinction coefficient at 280 nm. To be able to periodically inject fresh solutions, we kept the sam-

ple open and maintained a small flow of buffer during our experiments, which led to a slow drop in protein concentration. This drop in concentration was estimated separately from the fluorescence changes caused by flow-through of fluorescent proteins. Undesired sticking of microtubule tips to surfaces was prevented by coating the home-built flow chamber with agarose and BSA or casein.

Microtubule end mechanics. To estimate the reduction in effective length ΔL of a microtubule sheet or short protofilament under a compressive force F (figure 3.5 a), we use the following estimate of the extra amount of elastic energy that is stored in the sheet or filament:

$$\Delta E = \int_0^{L_{\max}} \frac{\kappa}{2}\left(\frac{1}{R_0} - \frac{1}{R_F}\right)^2 dl, \tag{3.1}$$

where R_0 is the preferred radius of curvature, R_F is the force-induced (smaller) radius of curvature, and κ is the stiffness of the sheet or protofilament. The projected length, on the direction of detection, of a curved sheet or filament is given by $L(R) = R\sin(L_{\max}/R)$, where $L_{\max}$ is the length of the sheet or filament when it is completely straight. We further use $\Delta L = L(R_0) - L(R_F)$ and $F = \Delta E/\Delta L$. From this we estimate that for a sheet length of 125 nm, with a preferred radius of curvature of 250 nm and estimated stiffness 100 times less than a microtubule, full closure of the sheet under a compressive force of 2.5 pN leads to an observed length increase of only a few nm. On the other hand, the addition of a 60 nm long oligomer (preferred radius of curvature of 76 nm and estimated stiffness 500 times less than a microtubule) leads to an increase of several tens of nm, even when it is not supported by lateral connections to other protofilaments and/or stiffened by an associated XMAP215 molecule.

3.3.2 Step fitting algorithm

Evaluating possible step-like processes in otherwise noisy data sets is a returning problem in many biophysics studies. With non-constant step sizes and small numbers of step events, a classical method like evaluating pairwise distance distribution functions does not suffice. Similarly, if there is no clear distinction between noise and very small steps, it is not straightforward to separate background noise from true molecular events. We developed a simple, practical algorithm that allows us to distinguish pronounced step-like behavior from gradual non-stepped growth, and to return the size distribution of the steps that are distinguishable from the noise (see for more details our published article [143]). The sole assumption we make is that the original data is a step train with steps of varying size and duration, hidden in Gaussian noise.

The step-fitting algorithm involves 3 steps:

1. Finding steps. The algorithm starts by fitting a single large step to the data, finding the size and location of this first step based on a calculation of the Chi-squared. Subsequent steps are found by fitting new steps to the plateaus of the previous ones, each time selecting the most prominent one first. This eventually leads to a series of 'best'

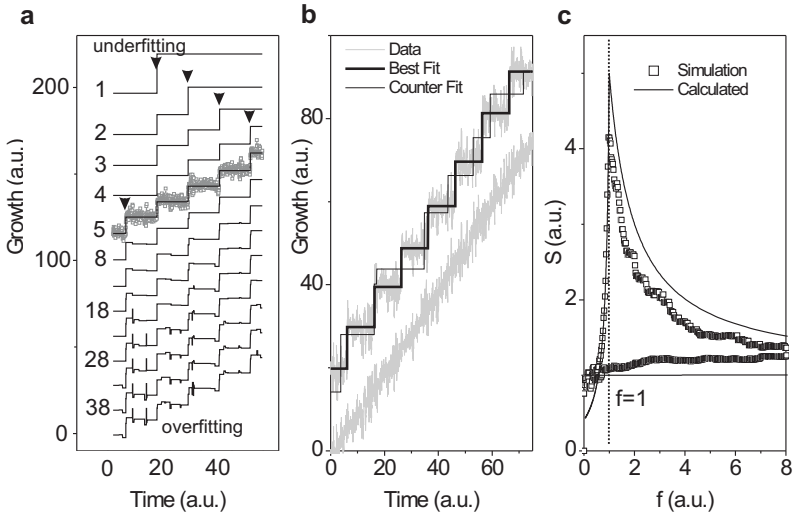

Figure 3.7: Step fitting procedure. **(a)** Iterations of the step-fitting algorithm on a simulated, noisy track of stepped data (step size 10 nm, RMS noise 2.5 nm). Curves are shifted vertically for clarity. The arrowheads point to every new step that is added to the fit. Underfitting means that significant steps in the data are not yet located, while overfitting means that merely noise is fitted. **(b)** A "best" fit (thick line) to noisy steps (step size 10 nm, RMS noise 2.5 nm) together with a "counter" fit (thin line, see text). The quality of these two fits differs strongly for a stepped signal, while for linear noisy growth (lower curve), the location of any step is arbitrary and the quality is equal. **(c)** Simulation result and calculation of the quality ratio S of best fit and counter fit, plotted vs. the relative number of fitted steps f. Upper curves are for a noisy stepped signal. Lower curve is for a noisy linear signal. S only peaks sharply if there are steps present, and if the correct number of steps is fitted (when $f = 1$).

fits that differ only by one step (figure 3.7 a). The fits with a very low number of steps are likely to underestimate or 'underfit' the real number of steps in the data, whereas the small steps that are added in the last iterations will merely be fitting the noise, thereby 'overfitting' the data.

2. Evaluating the quality of the step fits. Each best fit in the series is compared to a 'counter fit' that has an equal number of steps as the original one but with step locations in between the step locations found by the best fit (figure 3.7 b). We define a 'step-indicator' S as the ratio between the Chi-squared of the counter fit and the Chi-squared of the best fit. When the number of steps in the best fit is very close to the real number of steps in the data, the value of S will be large (figure 3.7 c). If however the data are severely under- or overfitted, or when the data consist of gradual non-stepped growth, the value for S will be close to 1.

3. Finding step distributions. To construct a histogram of the step sizes, an 'optimal' fit (the one representing best the real steps in the data) has to be chosen. Ideally this is the one with the number of steps that produces the highest value of S. In practice, we

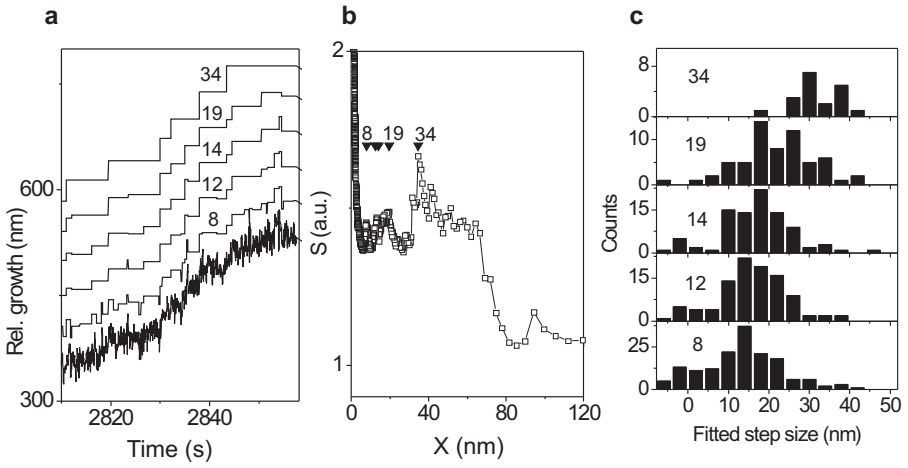

Figure 3.8: Fitting experimental data for pure tubulin growth. **(a)** Part of the raw data of a pushing microtubule with a series of increasingly finer step-fits. The numbers refer to the corresponding value of the parameter X, which represents the average size of the fitted steps. X is calculated as $X = L_{\mathrm{tot}}/N_{\mathrm{f}}$, where L_{tot} is the total length of the data trace and N_{f} is the number of fitted steps **(b)** S as a function of X for the complete data set, showing values above 1 over a wide range of length scales. Arrowheads and numbers refer to the specific step-fits shown in **(a)**. **(c)** Associated step-distributions. Step sizes up to 20 - 30 nm are found even when the data are clearly 'overfitted' (for $X = 8$). Note that overfitting mostly leads to the addition of alternating up and down steps.

usually choose a fit that appears to slightly overfit the data (see figure 3.8).

This procedure allows us to i) distinguish step-like growth from gradual non-stepped increases in length in a quantitative way, and ii) identify and quantify the steps that are distinguishable from the noise. The individual steps do not have to be equal in size or duration, and no a-priori assumptions about the signal to noise ratio are necessary. Of course, if the underlying steps are small compared to the noise, the algorithm will not be able to reliably distinguish a train of steps from linear non-stepped growth, which will manifest itself through a low value of S. If, as is the case for tubulin growth, the data consist of combinations of steps that are large and small compared to the noise, the algorithm will ensure that we find the sizes of the large ones. However, the optimal fit that we find based on the size of the large steps, will also put arbitrary steps on the rest of the data. A recent study compared the performance of different step detection methods and found that the Chi-squared based algorithm, developed in our group, is the simplest to optimize and has excellent temporal resolution [156].

In figure 3.8 we show the result of this procedure for the growth data with pure tubulin presented in this chapter. Note that in this case a substantial fraction of the growth occurs through steps that are indistinguishable from the noise and/or linear growth. Our algorithm is designed to find the sizes of steps that are distinguishable from the

noise, but also forces steps on the rest of the data. These last step sizes vary strongly when we vary the number of steps fitted to the data, but the 20 - 30 nm peak remains present even when we clearly start to overfit the data (figure 3.8 c).

3.4 Towards understanding the molecular mechanism of interaction between XMAP215 and tubulin

Our high-resolution observations suggested that XMAP215 might template formation of long tubulin oligomers. XMAP215 is an elongated protein that could accommodate along its length 7-8 tubulin dimers. Previously, it was shown that incubation of XMAP215 with tubulin at 4^oC yielded formation of tubulin partial rings in a complex with XMAP215 [64]. Results from microtubule binding studies suggest that XMAP215 comprises two tubulin binding domains: a 'high-affinity' domain (with dissociation constant $K_D < 1$ μM) near the middle of the protein and a 'moderate-affinity' domain ($K_D \approx$ 2-5 μM) broadly distributed near the N terminus [120, 157].

In an attempt to find out whether XMAP215 could bind multiple dimers along its length, at similar experimental conditions as the high-resolution measurements, we used fluorescently speckled microtubules and fluorescence correlation spectroscopy. The formation of tubulin oligomers with sizes comparable to the XMAP215 protein itself, should be easily observed with both methods. In our experiments, we did not identify big oligomers induced by the presence of XMAP215. An independent technique and further controls would be necessary to exclude a technical artifact. For example, the presence of the fluorescent dye on tubulin might interfere with the XMAP215-tubulin interaction. However, it is still possible that XMAP215 interacts with the fluorescently-labelled tubulin, but binds only 1-3 tubulin dimers. In this case both methods presented here would fail to identify the complex formation due to the limited resolution. Our results and observations are presented in this section.

3.4.1 Speckled microtubules

Fluorescence speckle microscopy (FSM) was developed to visualize movement, assembly and turnover of microtubules and actin filaments in living cells [158, 159]. When a low amount of fluorescently-labelled tubulin is microinjected into cells, microtubules appear 'speckled'. Both *in vivo* and *in vitro* experiments confirmed that microtubules obtain the fluorescent speckle pattern from the stochastic association of labelled and unlabelled tubulin subunits with the growing ends [160, 161].

We used FSM to investigate *in vitro* the assembly of microtubules in the absence and in the presence of XMAP215. XMAP215 was pre-incubated with the labelled fraction of tubulin. By analyzing the speckle pattern along microtubules we were aiming to gain information on the XMAP215-induced oligomerization of tubulin.

Principles of speckle image formation. Microtubules assemble by random association of tubulin subunits (figure 3.9 a). When a fraction f of labelled tubulin is present

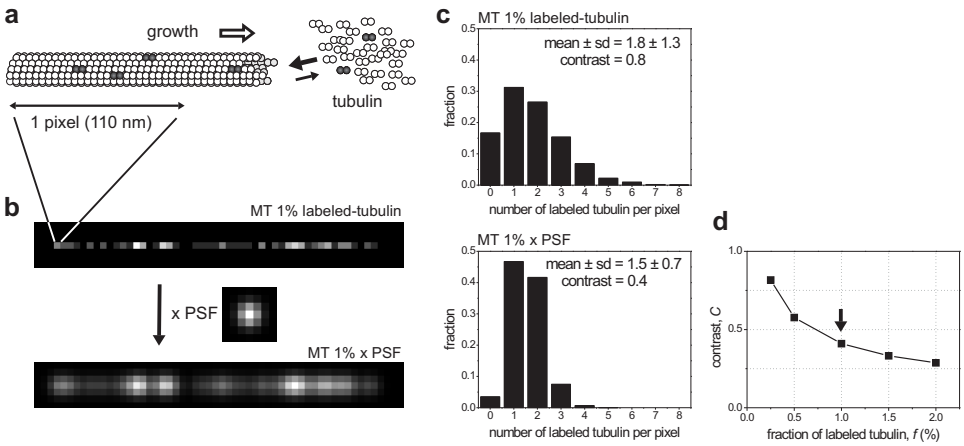

Figure 3.9: Speckle formation. **(a)** Schematic drawing of a microtubule growing in the presence of a small fraction of fluorescently labelled tubulin dimers. The microtubule elongates by random association of tubulin subunits at the growing end. **(b)** Pixel intensity along a theoretical microtubule 'grown' from a pool of tubulin containing 1% labelled tubulin. Each pixel corresponds to 110 nm microtubule length. The pixel intensity is given by the number of fluorescent subunits and was calculated using a discrete binomial distribution. The microtubule is 5.5 μm in length. When the theoretical microtubule is 'imaged' with our confocal microscope, the pixel distribution is convolved with the microscope point spread function (PSF). The PSF was experimentally determined from images of a surface sparsely coated with rhodamine-labelled tubulin. **(c)** Distributions of fluorescent subunits per pixel along microtubules, theoretically assembled at similar conditions with the ones shown in **(b)**. The distributions show the percentage of pixels with a corresponding number of fluorescent tubulin subunits and were constructed from theoretical microtubules with a total length of 550 μm. The convolution with the PSF reduces the pixel contrast, C = sd/mean. **(d)** Calculated speckle contrast, C, as a function of labelled-tubulin fraction.

in the tubulin pool, the fluorophore distribution along microtubules is described by a discrete binomial distribution (see Methods). The microtubule image through a microscope is a convolution of the fluorophore distribution along the microtubule with the point spread function (PSF) of the microscope. Figure 3.9 b shows an example of a theoretical microtubule and the effect of PSF on the speckle pattern.

The PSF of our confocal microscope can be approximated by a Gaussian with a standard deviation of 1 pixel (110 nm). One pixel corresponds in length to $N = 180$ tubulin dimers. As N is sufficiently high, the distribution of fluorescent dimers per pixel can be approximated with a normal distribution with a mean given by $\mathrm{m} = Nf$ and a standard deviation given by $\mathrm{sd} = \sqrt{Nf(1-f)}$. Speckle contrast was defined as $C = \mathrm{sd}/\mathrm{m} = \sqrt{(1-f)/(Nf)}$ [160], which can be approximated by $C = 1/\sqrt{Nf}$ for low fractions of fluorescent subunits, f. This formula suggests that the contrast, C, increases when decreasing the fraction of labelled tubulin, f (figure 3.9 d). In practice, how low f can be is limited by the fluorophore properties and the imaging system. The convolution with the PSF of the fluorophore distribution per pixel will effectively lower

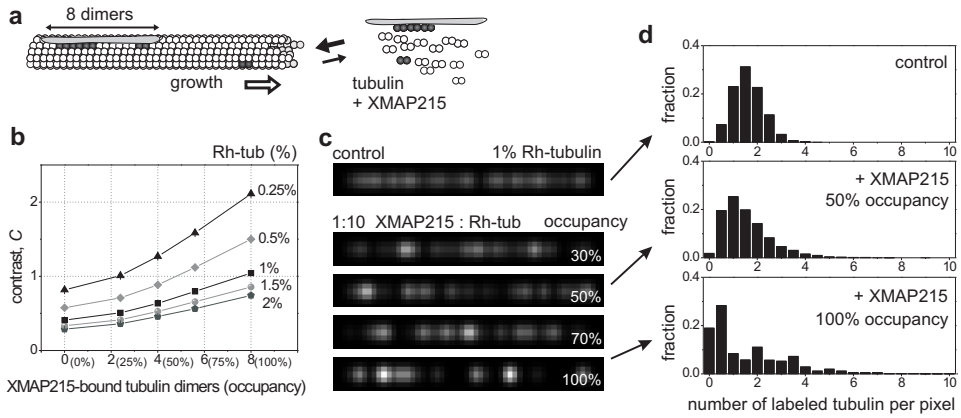

Figure 3.10: Theoretical speckled microtubules in the presence of XMAP215. **(a)** Schematic drawing of a microtubule assembled from a tubulin pool containing a small fraction of fluorescently labelled dimers that was pre-incubated with XMAP215. We assume here that XMAP215 forms stable complexes with the labelled tubulin that are subsequently incorporated into the growing microtubules. **(b)** Pixel contrast, C, as a function of the XMAP215 occupancy with labelled tubulin subunits. XMAP215-induced oligomerization results in increased speckle contrast. Calculations were performed using discrete binomial distributions (see Methods) for different labelled tubulin fractions, indicated in the graph. **(c)** Images and **(d)** pixel intensity distributions of theoretical microtubules assembled from 1% labelled tubulin in the absence and in the presence of XMAP215 in the pre-incubation step (1:10 XMAP215:labelled-tubulin). When more tubulin binds to XMAP215, fewer and brighter speckles are formed. Maximum occupancy corresponds to 8 tubulin dimers bound to each XMAP215 molecule. The distributions were determined from a total microtubule length of 550 μm.

the speckle contrast (figure 3.9 b and c). Previous studies found that the experimental optimal contrast is obtained when f is in the range of 0.5% to 2% [161, 162].

Calculated speckle distributions in the presence of XMAP215. In our experiments we pre-incubate the labelled tubulin fraction with XMAP215. Our hypothesis is that XMAP215 is inducing oligomerization of tubulin. We assumed that the labelled tubulin subunits bind stochastically to XMAP215 molecules and the XMAP215-tubulin complexes are stable and can incorporate into the growing microtubule. A fully occupied XMAP215 molecule carries 8 tubulin dimers, arranged in a straight line. In our calculations we considered several levels of XMAP215 occupancy with tubulin, occupancy defining the percentage of the molecule length filled with tubulin dimers. 50% occupancy means that, on average, 4 tubulin dimers are bound to one XMAP215 molecule. We further assumed that the number of dimers bound to each XMAP215 molecule also follows a discrete binomial distribution. The XMAP215 molecules carrying labelled-tubulin and the tubulin dimers not associated with XMAP215 bind stochastically to the growing microtubule end (figure 3.10 a).

Figure 3.10 shows the effect of XMAP215-induced oligomerization on the pixel intensity distributions. In our calculations we considered a ratio of XMAP215 to labelled

tubulin of 1:10, similar to the experimental conditions. For various labelled tubulin fractions, f, and XMAP215 occupancy, we determined an increase in the pixel contrast in the presence of XMAP215, as compared with the absence of the protein (figure 3.10 b). With XMAP215 we expect fewer, but brighter speckles along microtubules (figure 3.10 c and d).

Experimental results and discussion

We assembled microtubules in the presence of 0.5%-2% rhodamine-labelled tubulin (figure 3.11 a) and we compared the pixel intensity distributions along microtubules in the absence and in the presence of XMAP215.

The pixel intensity contrast and distributions measured in the absence and in the presence of XAMP215 in the pre-incubation step were very similar for all experimental conditions investigated. One example is shown in figure 3.11 b and compared with the expected difference in the theoretical distributions at similar conditions (figure 3.11 c). The difference predicted by the calculations are not observed in the experimental data. This observation could have several explanations. It is possible that upon dilution in the polymerization mix, the rhodamine tubulin bound to XMAP215 is exchanged with the unlabelled tubulin. In our experiments the amount of unlabelled tubulin in solution is typically 1000 fold higher than the amount of XMAP215 molecules. Therefore the kinetics of the XMAP215-tubulin interaction might favor the release of the labelled tubulin and rebinding of unlabelled dimers. The alternative explanation is that XMAP215 does not bind multiple tubulin subunits. We therefore used an additional technique (fluorescence correlation spectroscopy) to investigate directly the interaction between XMAP215 and tubulin in solution (section 3.4.2).

Methods

Theoretical distributions. The number of labelled tubulin dimers per pixel, the number of XMAP215 molecules per pixel, and the number of labelled tubulin bound to each XMAP215 molecule were determined using discrete binomial distributions.

The binomial distribution gives the discrete probability distribution $P_p(n|N)$ of obtaining exactly n successes (n subunits incorporated in a pixel-size length of a microtubule) out of N trials (total number of tubulin subunits comprised in a pixel-size length, $N = 108$ for a 110 nm pixel), where the result of each trial is true with probability p and false with probability $q \equiv 1 - p$. In our case, the probability p is given by the fraction, f, of labelled subunits or of XMAP215 molecules. The binomial distribution is therefore given by:

$$P_f(n|N) = \frac{N!}{n!(N-n)!} f^n (1-f)^{N-n} \tag{3.2}$$

The number of labelled tubulin dimers bound to each XMAP215 molecule is calculated in a similar way, with $N = 8$ and probability given by the occupancy (percentage of XMAP215 filled with dimers).

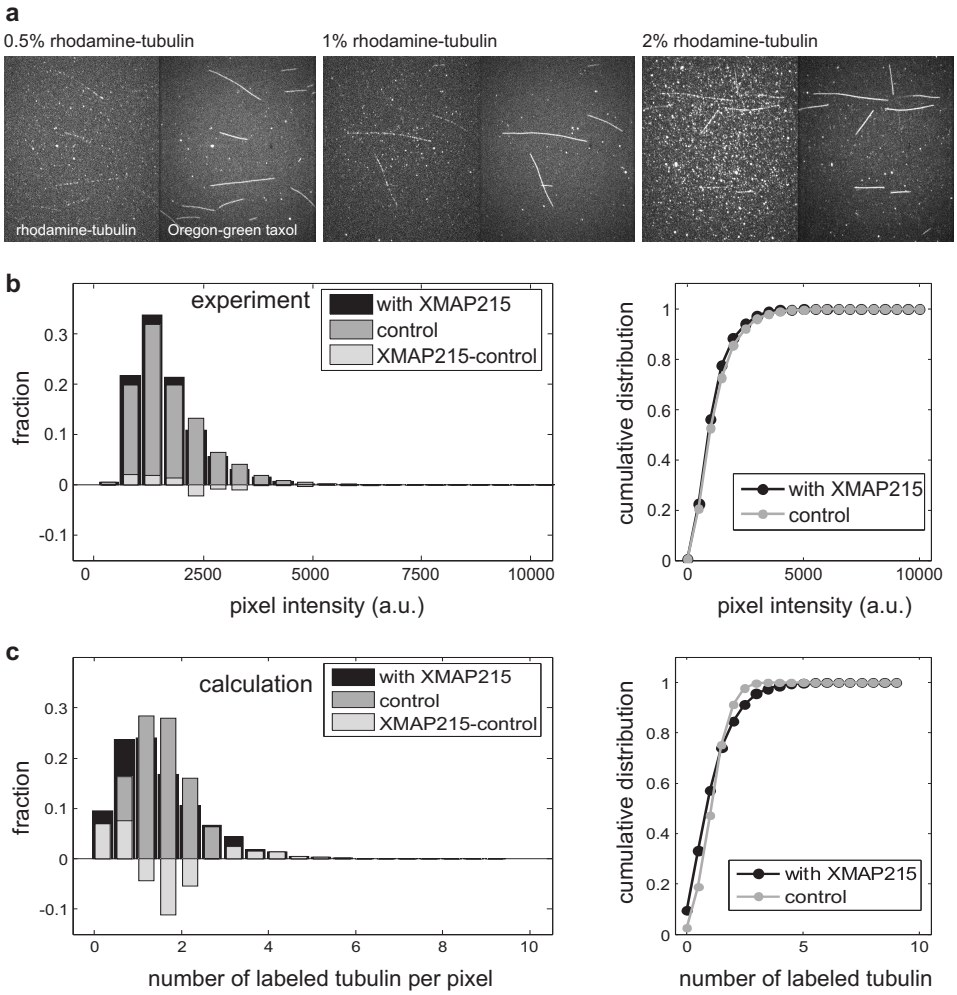

Figure 3.11: Speckled microtubules assembled *in vitro*. **(a)** Dual color images (rhodamine-tubulin and Oregon green taxol) of microtubules assembled from a tubulin pool containing indicated fractions of rhodamine-labelled tubulin. Microtubules were imaged with a spinning-disc confocal microscope. **(b)** Pixel intensity distributions and cumulative distributions for microtubules assembled in the absence and in the presence of XMAP215. XMAP215 was pre-incubated with the rhodamine-labelled tubulin in a ration of 1:10 XMAP215:tubulin. In the polymerization mix, the fraction of labelled tubulin was 1%. **(c)** Pixel intensity distributions and cumulative distributions calculated for theoretical microtubules assembled at similar conditions as in **(b)**. We assumed that each XMAP215 molecule had bound on average 4 tubulin dimers (50% occupancy).

In vitro assembly of speckled microtubules. Microtubules were assembled by incubation of 20 μM tubulin, containing 0.5%, 1%, or 2% rhodamine-labelled tubulin and 10% biotin-labelled tubulin, with 1 mM GMPCPP (Jena Bioscience, Germany) in MRB80 at 36°C for 50 minutes. In the XMAP215 containing samples, the fraction of rhodamine-labelled tubulin was pre-incubated with XMAP215 as follows. A mix of 5 μM rhodamine-tubulin, 0.5 μM XMAP215 and 1 mM GTP was incubated for a couple of minutes at room temperature or, alternatively, for up to 1 h on ice. After incubation, the XMAP215 mix was diluted in the polymerization mix to the final concentration of rhodamine-tubulin. The incubation was done in the presence of GTP to avoid artifacts of oligomer formation due to spontaneous nucleation. The microtubules were assembled in the presence of GMPCPP to suppress dynamic instability. In this way, the possible XMAP215-templated oligomers formed in the incubation step are locked in the microtubule lattice. Otherwise, in the presence of GTP, microtubules will undergo several polymerization-depolymerization cycles and the rhodamine-tubulin comprised in oligomers, if formed, would be randomized. After polymerization, the stable GMPCPP microtubules were diluted with a taxol solution containing 3 μM Oregon green-labelled taxol (Invitrogen) and 7 μM unlabelled taxol. The green taxol marks the entire length of the microtubule, allowing for microtubule localization when imaging the sample. Tubulin and unlabelled taxol were purchased from Cytoskeleton.

Confocal imaging of microtubules and pixel intensity distributions. Speckled microtubules were attached via streptavidin-biotin bonds to a functionalized surface. The surfaces of cleaned coverslips were covered with a compound layer of biotin-BSA and streptavidin as described in section 3.3.1. Microtubules were imaged with a dual-color spinning-disc confocal microscope, as described in section 4.3. Microtubules were localized by imaging the Oregon green taxol and a second image of the rhodamine-tubulin in the same field of view was recorded. Typical exposure was 2 s for the rhodamine image. Images were captured by a cooled EM-CCD camera (C9100, Hamamatsu Photonics) that has 16 μm square pixels and a 14 bit linear range of photon detection. Figure 3.11 a shows images of speckled microtubules grown at different fractions of rhodamine-tubulin.

Digital images were further analyzed in Matlab (MathWorks) to extract the pixel intensity distributions along microtubules. First, the images were corrected for the spatial illumination profile of our set-up, that had a 2D-Gaussian shape. Line profiles were drawn on the Oregon green-taxol images to localize the microtubules. The line coordinates were further used in the red-channel images to measure intensity line profiles of rhodamine-speckles on individual microtubules. One microtubule profile was the sum of three adjacent line scans to account for the PSF of the microscope. In one sample 30-90 microtubules were analyzed, comprising a total length of 200-500 μm.

3.4.2 FCS measurements on XMAP215-tubulin complex formation

Fluorescence correlation spectroscopy (FCS) allows for the determination of the diffusion characteristics of fluorescent molecules and their interaction with other particles [163]. We used FCS to measure diffusion coefficients of tubulin in dilute solutions in the absence and in the presence of XMAP215, in an attempt to investigate XMAP215-tubulin complex formation in solution.

Principles of FCS. In FCS the kinetics of fluorescent molecules are measured by monitoring the fluctuations of their emission intensity in a confocal excitation volume [164]. The detection volume is defined by the diffraction-limited focal spot of a strongly focused laser beam in combination with a confocal detection pinhole, leading to a Gaussian intensity profile. Fluorescent molecules enter and exit the excitation volume due to Brownian motion giving rise to fluctuations in the detected emission intensity. In FCS, the detection volume is typically in the femtoliter range, i.e. approximately the volume of a bacterial cell, and concentration of fluorescent molecules is in the nanomolar range, resulting in only a few molecules being present in the detection volume. The auto-correlation function, $G(\tau)$, of the recorded intensity signal is related to the characteristic diffusion time, τ_d, during which a molecule resides in the observation volume. Equation 3.3 gives the analytical form of the auto-correlation function when two populations of diffusing particles are present in solution:

$$G(\tau) = \frac{1}{N_1}\left(\frac{1}{1+\frac{\tau}{\tau_{d1}}}\right)\sqrt{\frac{1}{1+f^2\frac{\tau}{\tau_{d1}}}} + \frac{1}{N_2}\left(\frac{1}{1+\frac{\tau}{\tau_{d2}}}\right)\sqrt{\frac{1}{1+f^2\frac{\tau}{\tau_{d2}}}} \quad , \tag{3.3}$$

where N is the average number of fluorescent particles within the excitation volume and can be calculated, for a single diffusing species, from the initial correlation amplitude, $G(\tau \rightarrow 0) = 1/N$ (figure 3.12). f is the ratio between the axial, ω_z, and lateral, ω_{xy}, dimensions of the observation volume. ω_{xy} and ω_z denote the radii of the Gaussian profile at $1/e^2$ of its maximal intensity. In a calibrated observation volume with an exact Gaussian profile, $1/e^2$ radial dimension ω_{xy}, and known f, the diffusion coefficient, D, of a fluorescent species can be determined as $D = \omega_{xy}^2/4\tau_d$, where τ_d is evaluated from a fit to the auto-correlated signal (figure 3.13).

Results and discussion

Figure 3.12 shows the auto-correlation function of the fluorescence signal detected by FCS in an aqueous solution of 2.5 nM Rhodamine 6G. The diffusion coefficient of Rhodamine 6G is known, $D = 2.8 \times 10^{-10}$ m^2/s, at 20°C [166], and therefore we used the Rhodanime 6G samples to calibrate our system (determining ω_{xy} and f). The dimensions of the focal volume were determined from a one-component fit to the auto-correlation function (figure 3.13, left) and were typically found to be $\omega_{xy} = 470$ nm and $f = 10$ ($\omega_z = 4700$ nm). Figure 3.13, left, also shows the fit residual, representing the difference between the fitted and the measured autocorrelation function. The noisy

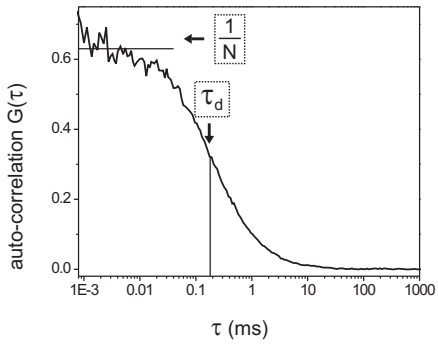

Figure 3.12: Auto-correlation function measured in FCS. The intensity signal was recorded in a solution of 2.5 nM Rhodamine 6G for 200s and fed into a hardware correlator that computes the auto-correlation of the signal as a function of the lag time τ. From the auto-correlation function, the number of particles in the detection volume, N, and the characteristic diffusion time of the particles in the detection volume, τ_d, can be determined (see text).

residual is flat indicating that our observation volume has a Gaussian shape. A wavy shape pattern present in the residual would indicate a non-Gaussian observation volume or a wrong assumption in the fitted function (for example a one-component fit of a signal from a two-component sample) [167].

In control samples we measured a diffusion coefficient for tubulin of (4.0 ± 0.3) x 10^{-11} m^2/s (table 3.2), similar to previously reported values measured using FCS [168]). The theoretically predicted value for the diffusion coefficient of a single tubulin dimer, 5.5 x 10^{-11} m^2/s (table 3.2), is somewhat higher than our measurements. One expla-

tubulin [nM]	XMAP215	ratio tub : xmap	D x 10^{-11} (m^2/s)
experiment			
0.2	-	-	4.0 ± 0.3
0.4	-	-	3.6 ± 0.1
0.2	+	3 : 1	3.4 ± 0.2
0.4	+	1 : 1	3.9 ± 0.5
theory			
tubulin dimer			5.5
XMAP215 + 1 tubulin dimer			3.9
XMAP215 + 7 tubulin dimers			1.7

Table 3.2: Diffusion coefficients of tubulin in the absence and in the presence of XMAP215. The experimental values were evaluated from a two-component fit to the auto-correlation function (see also figure 3.13). The diffusion coefficient of the fast component (free rhodamine) was fixed to 3.0 x 10^{-11} m^2/s. The theoretical values were calculated by using the formula for the translational diffusion coefficient of rod like molecules [165] (see also Methods).

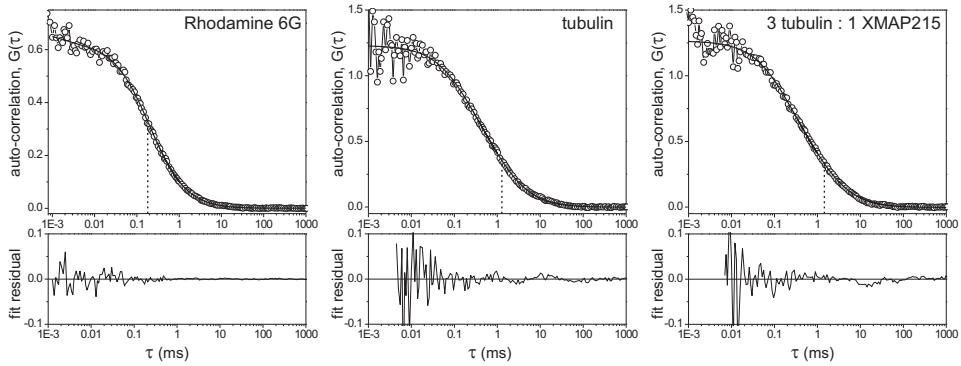

Figure 3.13: FCS measurement of tubulin-XMAP215 complex. The top panels show the auto-correlation function (open symbols) of the fluorescence signal recorded in a solution containing 2.5 nM Rhodamine 6G (left) and solutions containing 0.2 nM rhodamine-labelled tubulin in the absence and in the presence of XMAP215 (middle and right). The solid line is the respective two-component fit. The dotted lines indicate the characteristic diffusion time, τ_d, as evaluated from the fit. The lower panels show the difference between the auto-correlation function and the fit.

nation could be that the tubulin samples contain not only single dimers, but rather a mixed population of small oligomers that cannot be distinguished separately. The auto-correlation function and the residual are plotted in figure 3.13, middle. A two-component model was used to fit the experimental auto-correlation function, in order to account for the presence of free rhodamine dye (remainder from the tubulin labelling process). The diffusion coefficient of rhodamine (TAMRA, thetramethyl-rhodamine) was fixed to 3.0×10^{-11} m^2/s, value that was measured in a separate experiment. We noticed that the fit residual displays a wavy shape. This indicates the presence of multiple components in our sample, as we can exclude artifacts induced by a non-Gaussian shape of the observation volume (see the flat residuals in the case of a Rhodamine 6G sample, figure 3.13 left). There are limits, however, to the resolution of detecting multiple species. Theoretical and experimental studies show that the distinction between different molecular species depends on differences in their molecular brightness, size, and the concentration of each component in solution [169]. Molecules must differ in diffusion time by a factor of ~1.6 to be distinguished easily (more than 4 dimers in the case of tubulin, as estimated from calculations). From our FCS observations, if oligomers are present in the tubulin solution, their size must be small (2-3 dimers) or, if bigger, they represent a minority.

A theoretical calculation of diffusing particles predicts that a tubulin-XMAP215 complex would have a diffusion coefficient 1.4-fold lower when 1 tubulin dimer is bound to XMAP215 and up to 3.3-fold lower when 7 tubulin dimers are bound (table 3.2). Given the FCS resolution we would not be able to clearly identify XMAP215-tubulin complexes with less than 3-4 tubulin dimers bound to XMAP215. In the presence of XMAP215 we measured auto-correlation curves and diffusion coefficient of tubulin sim-

ilar to what we measured in the absence of XMAP215 (table 3.2). Figure 3.13 shows that the fit residual has also a slightly wavy pattern, similar to the tubulin solutions. As rationalized above, this indicates the presence of multiple components. The XMAP215-tubulin sample might contain a mixed population of tubulin single dimers, small oligomers, and XMAP215-tubulin complexes. We can not resolve whether these complexes are formed, but if so their size must correlate with only 1 or 2 tubulin dimers bound to XMAP215, given the limited resolution of FCS. If bigger oligomers or XMAP215-tubulin complexes are present, they represent a minority. It is also possible that XMAP215-tubulin complexes dissociate upon dilution to the nanomolar concentrations used in FCS. Another issue could be the presence of the fluorescent dye on tubulin, which could interfere with the interaction between XMAP215 and tubulin.

Further investigations are required to distinguish whether XMAP215-complexes are formed and to determine their typical size. A better option to study XMAP215-tubulin interaction using FCS is to measure nM labelled XMAP215 in the presence of μM concentrations of unlabelled tubulin.

Methods

Sample preparation. For the control samples, rhodamine-labelled tubulin (Cytoskeleton) was diluted to 6 μM in MRB80 supplemented with 1.2 mM GTP and 2.4 mg/ml BSA. The tubulin solution was centrifuged for 10 min at 16,100 x g at 4^{o}C to remove protein aggregates and further diluted to a final concentration of 0.2 nM or 0.4 nM in assay buffer (40 mM K-Pipes, 0.5 mM EGTA, 2 mM $MgCl_2$, pH 6.8) + 0.3 mg/ml BSA. According to the manufacturer, the labeling stoichiometry of tubulin is 1-2 dyes per tubulin dimer. In solution, we measured 20-30% free rhodamine dye from the total number of fluorescent molecules.

For the samples containing tubulin and XMAP215, rhodamine-labelled tubulin was diluted to 6 μM and centrifuged similar to the preparation for the control samples. The clarified tubulin (5 μM) was incubated for 1-2 min at room temperature with unlabelled XMAP215 at two different ratios of XMAP215:tubulin, 1:1 and 1:3. In this incubation step a total of 1 mM GTP and 2 mg/ml BSA was present in solution. The samples were further diluted to 0.2 nM or 0.4 nM tubulin, in a similar way as the control samples.

Diluted protein solutions were transferred into the wells of a glass bottom microplate (Whatman). The microplate wells used for measuring were first passivated, to reduce protein loss on surfaces, by incubation with 2.5 mg/ml BSA and subsequently rinsed with MRB80. All FCS measurements were performed in a sample volume of 100 μl at room temperature, 21±1^{o}C.

FCS measurements. Experiments were performed on a home-built FCS setup. The laser beam of a frequency doubled Nd:YAG laser at 532 nm (CrystaLaser) is coupled into an inverted optical microscope (Nikon Eclipse TE2000-U) and focused into the sample by a 63x 1.4 NA oil immersion objective (Nikon). The beam diameter was expanded through a two-lens telescope to slightly underfill the objective aperture. Fluo-

rescent signal from the sample and the excitation laser light are separated by a dichroic mirror (Chroma, z532rdc) in combination with a long-pass filter (Chroma, hq550lp) that blocks the remaining laser light reflected from the sample. The fluorescence light passes through a pinhole (50 μm in diameter), which blocks the photons produced outside the focal volume, and is detected by an avalanche photodiode (APD, Eg&G). The APD signal is fed into a hardware correlator (ALV/5000E), which computes the auto-correlation function of the fluorescence intensity signal.

Both the diameter of the excitation beam and the pinhole size have been chosen to minimize possible artifacts like a non-Gaussian intensity distribution in the focus [167]. Typical laser power at the sample was between 50-100 μW. In this regime the photobleaching should be negligible. The system was calibrated by collecting FCS curves of an aqueous solution of Rhodamine 6G molecules prior to each measurement. The auto-correlation of tubulin and tubulin-XMAP215 were typically recorded for 200 s and all samples were measured 3 times. The curves were further analyzed in Mathematica by fitting a two-component model (free dye and tubulin dimers) to determine the diffusion coefficients, D, of tubulin.

Theoretical diffusion coefficients of rod-like particles. We used a model described in [165]. For a cylinder of length L and diameter d, the translational diffusion coefficient, D, can be expressed as:

$$D = \frac{k_B T}{3\pi\eta L}\left(\ln\left(\frac{L}{d}\right) + 0.312 + 0.565\left(\frac{d}{L}\right) - 0.1\left(\frac{d}{L}\right)^2\right) \quad , \tag{3.4}$$

where $k_B T$ is the Boltzmann factor and η is the viscosity of the solvent. This model is correct for L/d approximately in the range 2 - 30. For the XMAP215-tubulin complexes we evaluated L from the total molecular volume and the average diameter, d, as estimated from published values.

3.5 Additional remarks and discussion

Two recently published studies [27,150] report additional information on the molecular details of microtubule growth and the interaction between XMAP215 and tubulin. Here our data is further discussed in the light of this new information.

At high spatial resolution, we measured fast length increases during microtubule polymerization corresponding to 2-3 tubulin dimers in size. The fast length increases could be caused either by instantaneous addition of small oligomers or subsequent addition of single dimers. We cannot resolve between the two possibilities due to the limited response time of our system (i.e. presence of drag forces on the bead-axoneme construct) and due to the time resolution of our detection method, limited to video rate. On the other hand, small tubulin oligomers are most probably present in our sample as we assembled microtubules in the presence of a relatively high amount of Mg^{2+} ions, which was previously shown to induce tubulin oligomerization [168]. Considering the presence of small oligomers and previous biochemical data suggesting that

GDP-tubulin can incorporate at the growing end [50, 170], we think that oligomer addition can be a mechanism contributing to microtubule elongation, as discussed earlier in this chapter (section 3.2). In contrast, a recent study by Scheck et al. [150] proposes that microtubule assembly takes place predominantly via single dimer addition. Using an optical tweezers based technique similar to the one presented in this thesis, the authors monitored microtubule assembly dynamics at high spatial and temporal resolution. However, the results from Scheck et al., and their interpretation thereof, cannot be directly compared with our results due to differences in the experimental conditions (tubulin concentration, Mg^{2+} ion concentration, temperature) and the differences between the two methods (nucleation sites used - axoneme vs microtubule and presence of an increasing force vs constant force against the microtubule, details that might affect the response time). Further experiments would be necessary to resolve the issue.

We also measured fast length increases during microtubule growth in the presence of XMAP215, with sizes up to the length of the XMAP215 protein itself. The sequence of molecular events underlying the XMAP215-catalyzed addition of tubulin at the growing end is still under discussion. We proposed two possible scenarios as exemplified in figure 3.5 b. One possibility is that XMAP215 templates formation of large oligomers in solution, which are subsequently incorporated at the growing microtubule tip, or XMAP215 first binds at the growing end where it facilitates addition of tubulin dimers along its length. Using FSM and FCS we did not detect formation of large oligomers in solution, although it was not clear whether we were not able to measure the large oligomers due to the experimental realization, e.g. low regime of protein concentrations and the presence of fluorescent dye on tubulin. Our FCS experiments suggested that, rather, only 2-3 dimers bind to XMAP215 in solution. Recently Brouhard et. al [27] also reported new insights into XMAP215-tubulin interactions by visualizing single XMAP215-GFP proteins interacting with dynamic microtubules. The authors propose that XMAP215 binds free tubulin in a 1:1 complex forming a closed configuration. The complex 'surfs' on the growing ends by a diffusion-facilitated mechanism, where it catalyzes the addition of multiple tubulin dimers (~300 at the specific experimental conditions). The idea that XMAP215 forms a complex with only 1 tubulin dimer correlates with our FSM and FCS observations. However, this idea is in contrast with previous experiments, where incomplete rings of tubulin in a complex with XMAP215 were observed to form in solution, the complex size matching the length of the XMAP215 protein [64]. However, taking into consideration our measurements in solution and the recently published data of Brouhard et. al, the second mechanism proposed by us could underly the fast length increases observed in our high-resolution data: XMAP215 at the tip facilitates the addition of tubulin subunits along its length. The multiple interaction sites between XMAP215 and tubulin would also insure the presence of the protein at the microtubule lattice for a while upon binding, supporting our observation of stepped depolymerization that indicates 'obstacles' on the microtubule lattice.

Acknowledgements
The major part of the work presented in this chapter is published in [143]. I would like to thank Jacob Kerssemakers, with whom I collaborated, for developing the experimental method and the step fitting algorithm and for performing first experiments together. I also thank Tim Noetzel, Kazuhisa Kinoshita and Tony Hyman for kindly providing the XMAP215 protein for us. For the FCS set-up and help with experiments I would like to thank Thomas Kalkbrenner and Sander Tans.

[143]: Kerssemakers JWJ, Munteanu EL, Laan L, Noetzel TL, Janson ME, Dogterom M (2006) Assembly dynamics of microtubules at molecular resolution. *Nature* **442**: 709-712